Title

Oxygen Vacancy Introduction to Increase the Capacity and Voltage Retention in Li-Excess Cathode Materials

Authors

Huang, Jianping

Zhong, Peichen

Ha, Yang

et al.

Oxygen Vacancy Introduction to Increase the Capacity and Voltage Retention in Li-Excess Cathode Materials

Jianping Huang, Peichen Zhong, Yang Ha, Zhengyan Lun, Yaosen Tian, Mahalingam Balasubramanian, Wanli Yang, and Gerbrand Ceder*

Li-rich rocksalt oxides are promising cathode materials for lithium-ion batteries due to their large capacity and energy density, and their ability to use earth-abundant elements. The excess Li in the rocksalt, needed to achieve good Li transport, reduces the theoretical transition metal redox capacity and introduces a labile oxygen state, both of which lead to increased oxygen oxidation and concomitant capacity loss with cycling. Herein, it is demonstrated that substituting the labile oxygen in Li-rich cation-disordered rocksalt materials with a vacancy is an effective strategy to inhibit oxygen oxidation. It is found that the oxygen vacancy in cation-disordered lithium manganese oxide favors high Li coordination thereby reducing the concentration of unhybridized oxygen states, while increasing the theoretical Mn capacity. It is shown that in the vacancy-containing compound, synthesized by ball milling, the Mn valence is lowered to less than $+3$, providing access to more than $300\,\text{mAh\,g}^{-1}$ capacity from the Mn^{2+}/Mn^{4+} redox reservoir. The increased transition metal redox and decreased O oxidation are found to improve the capacity and voltage retention, indicating that oxygen vacancy creation to remove the most vulnerable oxygen ions and reduce transition metal valence provides a new opportunity for the design of high-performance Li-rich rocksalt cathodes.

1. Introduction

The tremendous demand for high-energy batteries in electric vehicles necessitates the incorporation of inexpensive and earth-abundant elements in battery materials.[1] Current cathode materials in lithium-ion batteries are largely confined to the layered $Li(Ni,Mn,Co)O_2$ (NMC) compositional space,[2] where Co and Ni raise issues of high costs and resource scarcity.[1] Li-rich cation-disordered rocksalt (DRX) materials have drawn attention as alternative cathode materials because of their high compositional flexibility.[3–6] Inexpensive and abundant elements such as Mn and Ti can be incorporated into DRX cathodes and enable large capacity. For example, $Li_{1.2}Mn_{0.4}Ti_{0.4}O_2$ DRX delivers capacities in the range of 250–300 $\text{mAh\,g}^{-1}$ and a cathode energy density from 750 to 1000 $\text{Wh\,kg}^{-1}$, comparable to those of layered NMC cathodes though they require a larger voltage window to achieve this capacity, and currently still suffer from some capacity fade.[7–9] As in Li-excess layered materials,[10–13] the Li-excess used in DRX cathodes[5,7,8,14,15] reduces the amount of sites available for transition metal and hence the amount of transition metal redox capacity. For example, only 132 $\text{mAh\,g}^{-1}$ Mn^{3+}/Mn^{4+} redox capacity is available in $Li_{1.2}Mn_{0.4}Ti_{0.4}O_2$ and most of the practical capacity in this material is contributed by oxygen redox, similar to Li-rich layered NMC materials.[12,13] The oxygen redox activity can trigger oxygen loss, leading to capacity and voltage fade, as demonstrated in many Li-rich rocksalt or layered cathodes.[10,14,16–19] To achieve stable electrochemical cycling, a large capacity from the transition metal (TM) site is preferred. Several strategies can be deployed to increase the amount of transition metal redox capacity. High valent charge compensating elements, such as Ti^{4+}, Nb^{5+}, and Mo^{6+}, can be used to lower the transition metal valence.[4,14,20–22] Metals with a double redox couple can significantly increase the metal redox capacity when a limited number of metal sites are available.[4,13,20,22–25] Substitution of oxygen by fluorine in DRX materials has also been used as an effective strategy to mitigate oxygen loss and improve capacity and voltage retention.[4,14,18,26–28] The substitution of oxygen with fluorine increases TM capacity by increasing the redox-active TM content or by lowering the TM valence.[5] For example, the Ni^{2+} content

J. Huang, P. Zhong, Z. Lun, Y. Tian, G. Ceder
Materials Science Division
Lawrence Berkeley National Laboratory
Berkeley, CA 94720, USA
E-mail: gceder@berkeley.edu

P. Zhong, Z. Lun, Y. Tian, G. Ceder
Department of Materials Science and Engineering
University of California
Berkeley, CA, USA

Y. Ha, W. Yang
Advanced Light Source
Lawrence Berkeley National Laboratory
Berkeley, CA 94720, USA

M. Balasubramanian
Electrification and Energy Infrastructures Division
Oak Ridge National Laboratory
Oak Ridge, TN, USA

in $Li_{1.15}Ni_{0.375}Ti_{0.375}Mo_{0.1}O_2$ can increase from 0.375 to 0.45 when 0.15 O is substituted with F, which was shown to reduce the oxygen loss by 73%.[14] In Li_2MnO_2F, the Mn valence is lowered to +3, which significantly increases the reversible capacity from the Mn redox reservoir relative to that for Li_2MnO_3.[29]

In this work we push this strategy further and attempt to replace some oxygen ions by vacancies, which should be twice as effective in lowering the metal valence than fluorine substitution. In addition, prior theoretical and experimental work has demonstrated that the oxygen redox activity in rocksalt cathodes can be attributed to unhybridized oxygen with the Li–O–Li configuration.[30,31] Because these are the most weakly bonded oxygens, we speculate that vacancies may locate in these environments, and thereby remove some of the oxygens that are susceptible to oxidation. There is some evidence that oxygen vacancies can exist in rocksalt-like cathode materials. Chueh et al. recently reported that bulk oxygen vacancies can form and persist in layered $Li_{1.18}Ni_{0.21}Mn_{0.53}Co_{0.08}O_2$ during extended cycling.[32] Pralong et al. attempted to synthesize an oxygen-deficient $Li_4Mn_2O_5$ DRX by ball-milling $LiMnO_2$ and Li_2O and achieved a high initial capacity of 355 mAh g^{-1}.[33] However, continuous capacity and voltage fade ($\approx$30% capacity fade after only 8 cycles) were observed, which may be related to the limited Mn^{3+}/Mn^{4+} redox (corresponding to 246 mAh g^{-1}) and significant amount of oxygen redox.[33–35]

In this work, we implement the concept of oxygen vacancy introduction to achieve a large theoretical Mn redox capacity (353 mAh g^{-1}) in a cation-disordered $Li_5Mn_3O_{6.5}$ (LMO-V). The LMO-V cathode delivers a reversible capacity above 270 mAh g^{-1} for 25 cycles with negligible voltage fade (0.02 V),

which is in sharp contrast to stoichiometric $Li_5Mn_3O_8$ (LMO; 32% capacity fade and 7% voltage fade). Spectroscopic analysis indicates that the dominant Mn redox and minimal oxygen oxidation in LMO-V contribute to the improved cycle stability. The engineering of the oxygen stoichiometry in Li-rich rocksalt cathodes provides new opportunities for the manipulation of the cationic and anionic redox chemistry.

2. Results

2.1. Synthesis and Characterization of Stoichiometric and Nonstoichiometric Li–Mn–O

Stoichiometric LMO with a target Mn valence of +3.67 and oxygen-deficient LMO-V with a target Mn valence of +2.67 were synthesized using a mechanochemical ball-milling method. The Li excess of 25% in LMO-V can ensure good Li percolation[18] and the oxygen vacancy content helps maintain large theoretical Mn redox capacity. The relationship between Li content and theoretical capacity is summarized in Note S1, Figure S1, and Table S1, Supporting Information. Synchrotron X-ray diffraction (XRD) was used to characterize the phase purity in LMO and LMO-V. The XRD pattern of LMO, shown in **Figure 1**a, indicates the presence of the cation-disordered rocksalt phase (Fm-3m) without any apparent impurity peaks. The lattice constant was determined by Rietveld refinement to be 4.096 Å. The XRD pattern of LMO-V, Figure 1b, similarly shows characteristic diffraction peaks from the cation-disordered rocksalt phase, but with a few weak impurity peaks. Rietveld refinement indicates that the
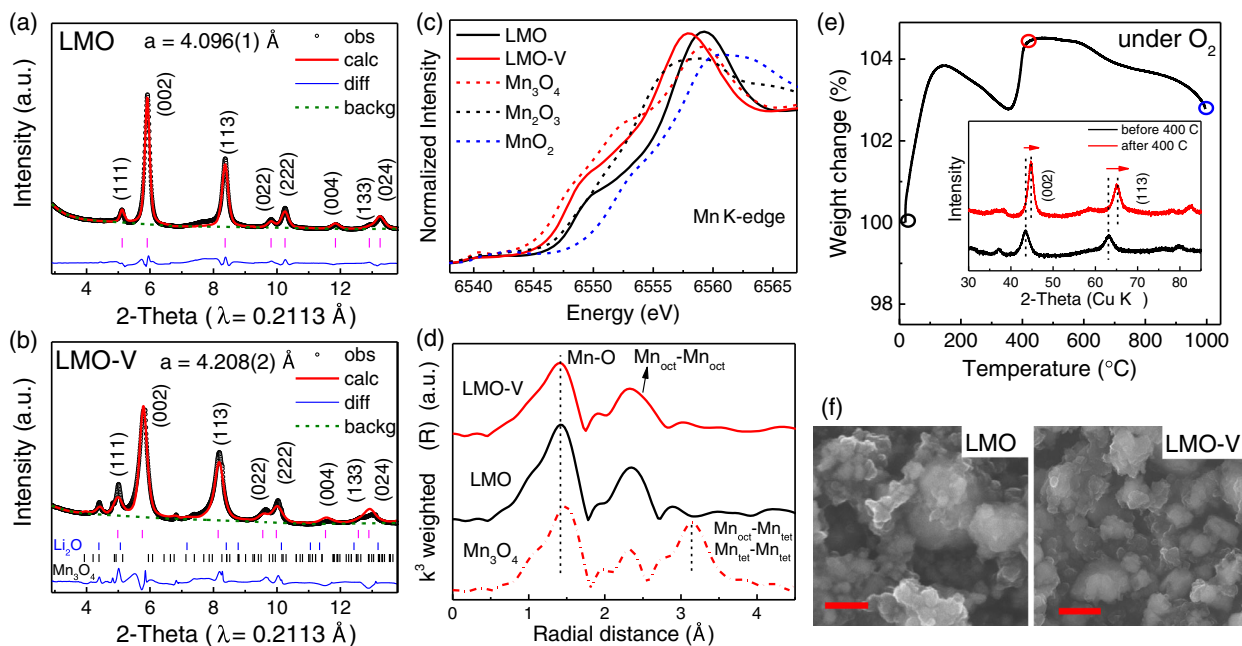

Figure 1. Structure characterization of $Li_5Mn_3O_8$ and $Li_5Mn_3O_{6.5}$. a) Synchrotron-based XRD patterns and refinement results of (a) $Li_5Mn_3O_8$ (LMO) and b) $Li_5Mn_3O_{6.5}$ (LMO-V). c) Mn K-edge XANES spectra of LMO and LMO-V. The spectra of Mn_3O_4, Mn_2O_3, and MnO_2 standards are plotted as dashed lines. d) Mn K-edge EXAFS spectra of LMO, LMO-V, and Mn_3O_4. The peaks in the radial distance range of 1–2 and 2–4 Å correspond to the Mn–O and Mn–Mn coordinations, respectively. e) Thermogravimetric profile of LMO-V at a heating rate of 5 °C min^{-1} under oxygen atmosphere. The inset presents the XRD patterns of LMO-V before TGA measurement and after heating to 400 °C. f) SEM images of LMO and LMO-V. Scale bar: 500 nm.

**ADVANCED
SCIENCE NEWS**

www.advancedsciencenews.com

**small
structures**

www.small-structures.com

disordered rocksalt phase (lattice constant: 4.208 Å) is dominant in LMO-V ($\approx$91%), with the impurity minority phases identifiable as remaining precursor Li_2O (5%) and Mn_3O_4 (4%). The presence of unreacted Li_2O was also previously observed by synchrotron XRD in the reported oxygen-deficient material $Li_4Mn_2O_5$.[34] Based on the weight percentages of the unreacted precursors obtained from the XRD, the molar ratio of the reacted $Li_2O:Mn_3O_4$ is 2.23:1, yielding an oxygen deficiency of approximately 16% in LMO-V.

The Mn valence in LMO and LMO-V was determined using Mn K-edge X-ray absorption near-edge structure (XANES) spectroscopy (Figure 1c). The Mn K-edge position of LMO is located between that of Mn_2O_3 (Mn^{3+}) and MnO_2 (Mn^{4+}). The Mn K-edge position of LMO-V is similar to that of Mn_3O_4 ($Mn^{2.67+}$) yet with a different edge shape, reflecting the different Mn coordination environment in LMO-V from that in the Mn_3O_4 precursor. The Mn valence was estimated from linear combination fits of the XANES spectra of Mn standards.[36] This leads to an assignment of Mn valance of $+3.4(\pm0.1)$ and $+2.80(\pm0.09)$ in LMO and LMO-V, respectively, close to the targeted Mn valences of the two compounds. The local structure in each compound was analyzed using Mn K-edge extended X-ray absorption fine structure (EXAFS) spectroscopy (Figure 1d). The similarity of the peaks at $\approx$1.5 and $\approx$2.5 Å in the EXAFS spectra of LMO and LMO-V indicates a similar local coordination environment in both compounds. These peaks can be assigned to Mn–O and octahedral Mn–octahedral Mn, respectively.

Thermogravimetric analysis (TGA) under an oxygen atmosphere (Figure 1e) shows a weight increase of $\approx$4.5% upon heating LMO-V to 400 °C. The small weight loss from 200 to 300 °C may be related to the desorption of some surface adsorbed species, which we were not able to characterize. Similar observations have been made in rare-earth manganites ($Dy_{1-x}Y_xMnO_{3+\delta}$).[37,38] The XRD pattern of the sample heated to 400 °C (inset of Figure 1d) shows that the cation-disordered rocksalt structure mostly remains present after heating. The (002) diffraction peak is shifted to 43.4° (from 44.7°) and the (113) diffraction peak shifted to 65.1° (from 63.1°) in the heat-treated LMO-V, indicative of a decreased lattice constant consistent with oxidation. Upon heating to 1000 °C under an oxygen atmosphere, the disordered-rocksalt structure of LMO-V transformed to monoclinic Li_2MnO_3, as evidenced by the XRD pattern (Figure S2, Supporting Information). The scanning electron microscopy (SEM) images of LMO and LMO-V (Figure 1f) reveal similar particle sizes of approximately 200 nm for the two samples.

2.2. Electrochemistry of LMO and LMO-V

The electrochemistry of LMO and LMO-V was compared in Li cells using galvanostatic charge/discharge tests. LMO delivers an initial discharge capacity of 334 mAh g^{-1} and an energy density of 998 Wh kg^{-1} at 20 mA g^{-1} in the voltage window of 5.0–1.5 V (**Figure 2**a). Under the same test conditions, LMO-V delivers a discharge capacity of 317 mAh g^{-1} and an energy density of 921 Wh kg^{-1} (Figure 2b). Both samples have excellent specific energy approaching 1000 Wh kg^{-1}, comparable to or larger than that of previously reported high-energy cathode materials.[4,29,39] In the first charge, LMO-V shows a lower voltage than LMO, consistent with the lower Mn valence in LMO-V. In particular, LMO-V shows a charge capacity of $\approx$300 mAh g^{-1}
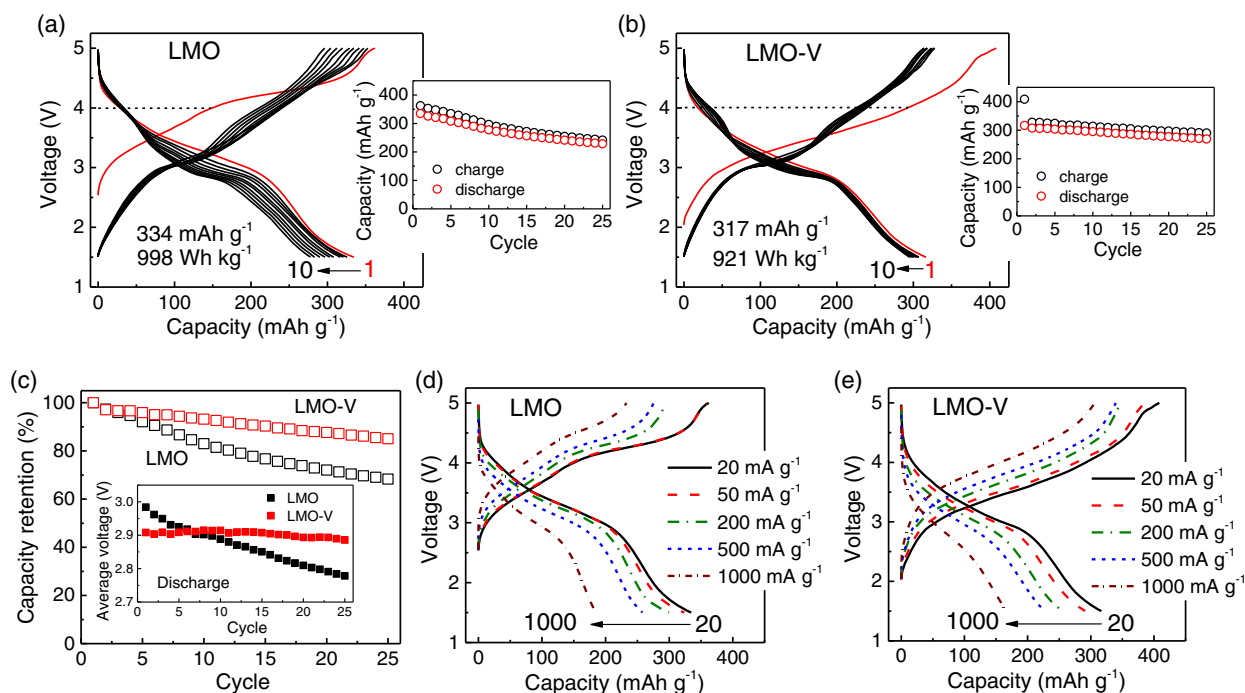

Figure 2. Electrochemistry of LMO and LMO-V at room temperature. Voltage profiles of a) LMO and b) LMO-V at 20 mA g^{-1} in the voltage window of 5.0–1.5 V. The insets show the capacity retention of the samples over 25 cycles. c) Capacity retention of LMO and LMO-V as a function of cycle number. The inset shows the average discharge voltages of LMO and LMO-V. First-cycle voltage profiles of d) LMO and e) LMO-V at different current densities.

(≈73% of the total charge capacity) below 4.0 V, whereas LMO's charge capacity below 4 V was ≈140 mAh g^{-1} (≈40% of the total charge capacity). Upon electrochemical cycling, apparent voltage and capacity fading were observed in LMO with the discharge capacity of LMO decreasing to 228 mAh g^{-1} at cycle 25 (1.3% fade per cycle), and the average discharge voltage continuously decreasing from 2.98 to 2.78 V (Figure 2c). In contrast, LMO-V averaged only 0.6% capacity loss per cycle maintaining a capacity of 269 mAh g^{-1} at cycle 25. The average discharge voltage for LMO-V only slightly decreased from 2.91 to 2.89 V. In the smaller voltage window of 4.4–2.0 V, LMO-V shows good capacity retention (95%) with capacity >130 mAh g^{-1} for 100 cycles (Figure S3, Supporting Information). These results all indicate that the introduction of oxygen vacancies is conducive to improving capacity and voltage retention in Mn-based DRX cathodes. The rate capability of LMO and LMO-V was compared at different current densities ranging from 20 to 1000 mA g^{-1} (Figure 2d,e). At 1000 mA g^{-1}, LMO delivers a capacity of 186 mAh g^{-1} (56% of its capacity at 20 mA g^{-1}), similar to LMO-V's capacity of

167 mAh g^{-1} at 1000 mA g^{-1} (53% of the capacity at 20 mA g^{-1}). The similar rate performance can be attributed to their similar excess Li (25%) which is critical to Li percolation in DRX materials.[6,18] At all different current densities, LMO-V consistently maintained higher capacity retention than LMO (Figure S4, Supporting Information).

2.3. Redox Mechanism and Structural Change

To understand the different electrochemistry in LMO and LMO-V, the redox mechanism was probed using hard X-ray absorption spectroscopy (XAS) and soft X-ray mapping of resonant inelastic X-ray scattering (mRIXS).

The Mn redox was further analyzed using Mn K-edge XANES spectroscopy (**Figure 3**a–c). As the charge capacity increases from 0 to 200 mAh g^{-1}, the Mn K-edge of LMO shifts from an energy between that of Mn_2O_3 and MnO_2 to an energy close to that of MnO_2, indicative of Mn oxidation from +3.4 to +4.0. Very little change was observed in the XANES spectrum upon further
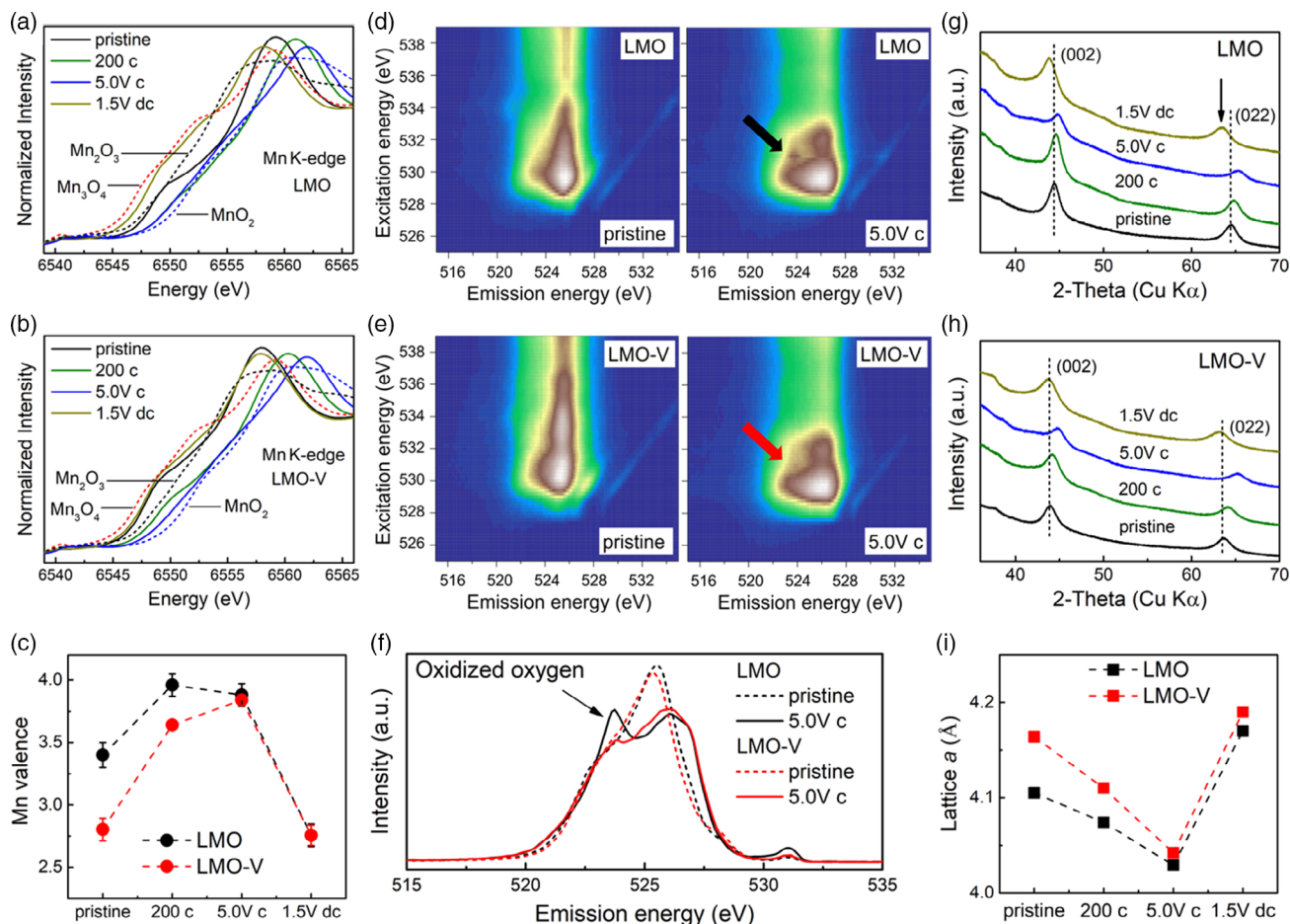

Figure 3. Redox mechanism and structural change of LMO and LMO-V. Mn K-edge XANES spectra of a) LMO and b) LMO-V in pristine, 200 mAh g^{-1}-charged, 5.0 V-charged, and 1.5 V-discharged state. The spectra of Mn_3O_4, Mn_2O_3, and MnO_2 standards are plotted as dashed lines. c) Quantified Mn valence of LMO and LMO-V using linear combination fitting of the XANES spectra. O K-edge RIXS map of d) LMO and e) LMO-V in pristine and 5.0 V-charged state. f) RIXS spectra collected at an excitation energy of 531 eV. The peak at an emission energy of 523.8 eV is a characteristic feature of oxidized oxygen. Ex-situ XRD patterns of g) LMO and h) LMO-V. i) Refined a-lattice parameters of LMO and LMO-V in pristine, 200 mAh g^{-1}-charged, 5.0 V-charged, and 1.5 V-discharged state.

charging to 5.0 V. The Mn K-edge of the 1.5 V-discharged LMO shifts to a lower energy position (close to Mn_3O_4) than that of the pristine state of LMO, indicating some irreversibility in LMO (Figure 3a). In contrast, LMO-V shows more reversible Mn redox upon charging/discharging. Upon charging to 5.0 V the Mn K-edge of LMO-V gradually shifts to an energy close to that of MnO_2 and completely shifts back to that of the pristine state upon discharging to 1.5 V (Figure 3b). The quantitative Mn valence was estimated by linear combination fitting of the XANES spectra of Mn standards (Figure 3c). This led to an assignment of Mn valence in LMO of $+3.4(\pm0.1)$, $+3.88(\pm0.09)$, and $+2.76(\pm0.09)$, respectively, in the pristine state, the top-of-charge state, and the 1.5 V-discharged state. The excessive reduction of Mn likely originates from irreversible oxygen loss[17,40] or possibly from overdischarge. On the other hand, the XANES spectra indicate that Mn in LMO-V is oxidized from $+2.80(\pm0.09)$ to $+3.84(\pm0.04)$ in going from the pristine to the top-charge state, and is back reduced to $+2.76(\pm0.08)$ in the 1.5 V-discharged state, indicating reversible Mn redox.

To evaluate the oxygen activities, we performed O K-edge mRIXS analysis (Figure 3d–f). mRIXS has become the tool-of-choice in detecting the chemical state of oxidized oxygen in a compound.[41,42] The feature with excitation energy of ≈531 eV and emission energy of 523.8 eV has been verified to be the fingerprint of the oxidized oxygen species.[41,42] The O mRIXS shows a clear characteristic signal of oxidized oxygen in the 5.0 V-charged LMO (Figure 3d black arrow) but the feature is negligible in the 5.0 V-charged LMO-V (Figure 3e). To facilitate a direct comparison, the RIXS cuts at 531 eV excitation energy are plotted in Figure 3f. The characteristic peak signal at 523.8 eV is much weaker in the 5.0 V-charged LMO-V than that in the 5.0 V-charged LMO, indicating significantly less oxygen oxidation relative to that in LMO. Note that the Mn^{3+}/Mn^{4+} oxidation in LMO can maximally contribute a capacity of ≈147 mAh g^{-1}, whereas an actual charge capacity of 362 mAh g^{-1} was achieved. Thus, the majority of the initial charge capacity in LMO should originate from oxygen oxidation, as supported by the RIXS results.

The bulk structural changes in LMO and LMO-V after charge and discharge were characterized using ex situ XRD (Figure 3g–i). The diffraction peaks of LMO shifted to higher angles upon charging, indicating a decrease of the lattice constant from 4.11 to 4.03 Å from the pristine to the top-charge state. Discharging to 1.5 V shifts the diffraction peaks back to lower angles, but to a position corresponding to an increased lattice constant of 4.17 Å, $\approx1.5\%$ larger than that in the pristine state. The larger lattice constant of the 1.5 V-discharged LMO is consistent with excess reduction of Mn upon discharge of LMO (Figure 3c). In contrast, LMO-V exhibited a more reversible lattice change, with the lattice constant decreasing from 4.16 to 4.04 Å upon charging and increasing to 4.19 Å upon discharging.

3. Discussion

3.1. Reduced Oxygen Oxidation

Oxygen redox is a common phenomenon in Li-rich rocksalt cathode materials;[31,39,43,44] however, surface oxygen loss and its associated reactions with the electrolyte can lead to performance degradation (e.g., capacity and voltage fade).[10–12] To mitigate the issues associated with oxygen oxidation, we demonstrated in this work that introducing oxygen vacancies can significantly increase the transition metal redox capacity and decrease O redox in a cation-disordered lithium manganese oxide. With the presence of oxygen vacancies, the Mn valence in LMO-V is lowered to ≈2.8, and a high capacity (>310 mAh g^{-1}) is available from the Mn redox reservoir. Moreover, oxygen vacancies can potentially reduce the concentration of the unhybridized Li–O–Li configurations, which facilitate the oxygen oxidation.[19,30,31] By reducing such states through oxygen vacancies, the first-cycle voltage hysteresis is significantly suppressed in LMO-V.[13]

Rocksalt cathodes have random cation arrangements and unhybridized Li–O–Li state mainly exists in Li-rich coordination environments (Li_6O, $MnLi_5O$, and Mn_2Li_4O). Some examples of these environments are shown in **Figure 4a**. If vacancies preferentially were to substitute these oxygen sites, the amount of unhybridized Li–O–Li states could be reduced. Such a preference of the oxygen vacancy for Li-rich environments can be expected as the covalency of the TM with oxygen leads to a higher binding energy than for Li–O. In a fully randomized system (cations randomly distributed as well as oxygen/vacancies), approximately 60% oxygen vacancies are present in the Li-rich environments. To estimate the distribution of oxygen vacancies more realistically, a cluster expansion Monte Carlo simulation was implemented at $T^* = 2100$K using effective interactions derived from density functional theory (DFT) calculations as in previous work on DRX oxides[45,46] (see details in the Experimental Section). The frequency by which different Li coordination numbers are found around oxygen vacancies was averaged over 1000 structures sampled from the equilibrium ensemble. The resulting distribution of lithium around oxygen vacancies is presented in Figure 4b. The data show a clear increase (decrease) of the vacancy environments with higher (lower) Li content in the ab initio simulation over the random ion distribution. Approximately 72% of oxygen vacancies are coordinated with at least four Li atoms in the ab initio simulation. This result is consistent with our intuition for the TM—O versus Li—O bond energy.

The schematic density of states of LMO and LMO-V are compared in Figure 4c. The Mn valence in LMO is approximately $+3.4$, creating limited electron occupation in the Mn e_g^* state. The unhybridized Li–O–Li state lies at higher energy than the fully hybridized oxygen state (O $2p$), which can lead to some overlap between the Mn e_g^* and Li–O–Li states.[31] Thus, the use of large charging capacity in LMO is likely to lead to the oxidation of oxygen. The lower Mn valence ($\approx+2.8$) in LMO-V creates higher electron occupation in the Mn e_g^* states, and the preference of the oxygen vacancy to be in Li-rich environments decreases the concentration of the unhybridized Li–O–Li state. Thus, the oxidation of LMO-V mainly involves the electrons in the Mn e_g^* state with only a minor contribution from the labile Li–O–Li state.

The irreversibility of oxygen oxidation can affect the redox behavior of the TM. For example, oxygen loss from layered $Li_{1.2}Ni_{0.15}Co_{0.1}Mn_{0.55}O_2$ yields low-valent Mn^{2+}/Mn^{3+} and Co^{2+}, which lower the overall charge/discharge voltage, leading
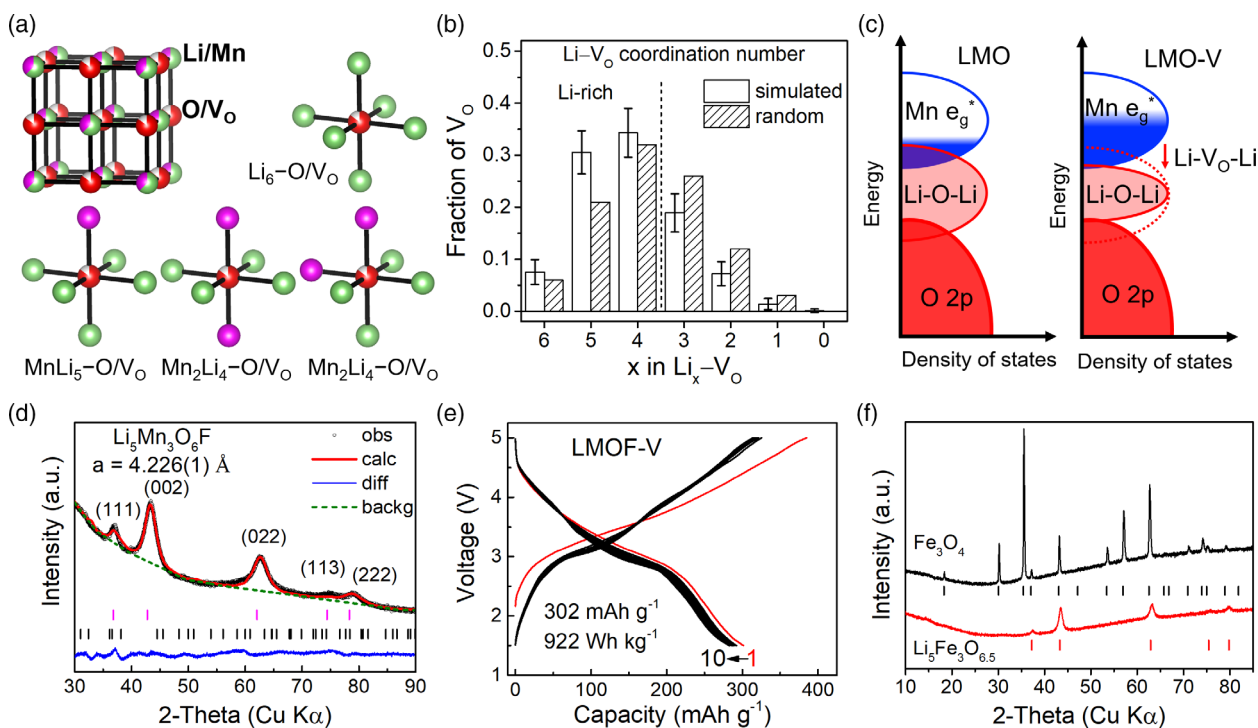
Figure 4. Rationalization of oxygen vacancy effect and its application in other DRX materials. a) Rocksalt structure of LMO-V in a random environment. Li, Mn, O, O-vacancy (V_O) are in green, magenta, red, and white, respectively. Unhybridized Li–O–Li configuration is present in Li-rich coordination environments (Li_6O, $MnLi_5O$, and Mn_2Li_4O), where oxygen vacancy can remove such unhybridized oxygen state. b) Distribution of Li–V_O coordination in LMO-V. The distribution in simulated and random structures is plotted as open and dashed bars, respectively. (c) Schematic plots showing band structures of LMO and LMO-V. d) XRD pattern of $Li_5Mn_3O_6F$ (LMOF-V). e) Voltage profiles of LMOF-V at 20 mA g^{-1} in the voltage window of 5.0–1.5 V. f) XRD patterns of Fe_3O_4 and $Li_5Fe_3O_{6.5}$ (LFO-V).

to voltage fade.[12] Notably, the Mn K-edge XANES results in this study also show a decrease of the Mn valence in LMO from ≈3.4 (pristine state) to ≈2.8 (1.5 V-discharged state) after a full discharge. The decreased Mn valence after charge and discharge is likely to be the cause of the decreasing average discharge voltage from 2.98 to 2.78 V (Figure 2c). Additionally, any oxygen loss generally renders the particle surface rich in transition metals, which has been referred to as surface densification[10,47] in prior studies of DRX materials.[20] The higher impedance of the densified area can cause increased polarization.[15,20] The polarization in LMO and LMO-V was therefore analyzed using the voltage difference (ΔV) between the average charge voltage and discharge voltage (Figure S5, Supporting Information). LMO shows a ΔV increase from 0.57 to 0.70 V from cycle 2 to cycle 25, whereas LMO-V shows minor ΔV increase from 0.57 to 0.59 V, indicating smaller polarization in LMO-V than in LMO. Overall, the reduced oxygen oxidation in the oxygen-vacancy-containing Li-rich DRX cathode seems to prevent reduction of the TM, and the concomitant polarization increase, contributing to the improved capacity and voltage retention.

3.2. Oxygen Deficiency in Other DRX Cathodes

The presence of oxygen vacancies in LMO-V lowers the Mn valence as well as the average voltage (2.91 V). To increase the voltage while maintaining the large Mn redox reservoir, we

partially substituted the oxygen and oxygen vacancies with fluorine in $Li_5Mn_3O_{6.5}$ (LMO-V) and prepared cation-disordered $Li_5Mn_3O_6F$ (LMOF-V) with the same target Mn valence (+2.67) as LMO-V. The refined XRD results reveal a major disordered rocksalt phase (98%, $a = 4.226$ Å) and a small amount of Mn_3O_4 (2%) (Figure 4d). LMOF-V delivered an initial discharge capacity (energy density) of 302 mAh g^{-1} (922 Wh kg^{-1}) when cycled between 1.5 and 5.0 V at 20 mA g^{-1}, with minor capacity and voltage fade observed upon cycling (Figure 4e). The first-cycle voltage profiles of LMOF-V were found to be higher than those of LMO-V (Figure S6, Supporting Information), and the average discharge voltage of LMOF_V (3.05 V) was 0.14 V higher than that of LMO-V, confirming the voltage increase upon fluorination. Notably, LMOF-V showed ≈50 mAh g^{-1} higher capacity than the previously reported stoichiometric $Li_5Mn_3O_{5.3}F_{2.7}$ under similar electrochemical test conditions.[18]

We demonstrate that oxygen vacancies can also be introduced into an Fe-based DRX material. Cation-disordered $Li_5Fe_3O_{6.5}$ (LFO-V) was prepared by ball-milling Li_2O and Fe_3O_4, with no apparent impurities in the XRD pattern (Figure 4f). Unlike Mn redox, which allows Mn^{2+}/Mn^{4+} double redox, Fe redox is generally limited to Fe^{2+}/Fe^{3+} in LFO-V. An initial discharge capacity of 206 mAh g^{-1} was delivered at 20 mA g^{-1} in the voltage window of 5.0–1.5 V (Figure S7, Supporting Information). The successful preparation of LFO-V indicates that it is possible to incorporate oxygen vacancies into other DRX materials for

compositional optimization. Prior investigations of oxygen vacancies in layered Li-rich cathodes have similarly shown improved electrochemistry.[48,49] For example, oxygen-deficient Li_2MnO_{3-x} $(0 < x < 0.19)$ delivered an initial discharge capacity of 310 mAh g^{-1}, which decreased to $\approx$240 mAh g^{-1} at cycle 10; in sharp contrast to stoichiometric Li_2MnO_3 for which the initial capacity decreased from $\approx$310 to $\approx$20 mAh g^{-1} after ten cycles.[49]

To further validate the idea that oxygen vacancies can be introduced into LMO, we used ab initio computations to evaluate the free energy cost of creating oxygen vacancies to create LMO-V. Figure S8, Supporting Information, shows the free energy of LMO-V and that of the competing stable phases in the Li–Mn–O phase diagram. This approximate analysis indicates that the configurational entropy of the LMO-V phase stabilizes it against decomposition into competing phases for $T \geq 1000$ K. Given that previous studies have indicated that ball milling can introduce disorder "equivalent" to that achieved $>1500\,°C$,[50] it seems feasible to achieve the LMO-V phase with high energy ball milling. While we did not attempt other strategies beyond ball milling to create the metastable oxygen vacancy-containing state, other processing techniques such as low-temperature annealing with agents which can remove lattice oxygen, such as LiH, NH_3, and CO_2,[48,49,51] may also be feasible. In addition, appropriate characterization techniques should also be explored for accurate quantification of the oxygen stoichiometry.

In conclusion, we demonstrated that the oxygen stoichiometry can be modified in cation-disordered lithium-rich manganese oxides via a mechanochemical method. The oxygen deficiency lowers the Mn valence and reduces the concentration of the unhybridized oxygen state that is inherent in Li-rich systems, which in combination increase the Mn redox and decrease the O redox. As a result, the oxygen-vacancy-containing lithium-rich manganese oxide delivers a high Mn-based capacity of >300 mAh g^{-1} with significantly reduced oxygen oxidation. The large Mn-redox reservoir and low amount of oxygen oxidation contribute to the improved capacity and voltage retention. The demonstration of a nonstoichiometric rocksalt cathode provides a new direction for compositional modifications in the chemical space of cation-disordered Li–TM–O/F. We believe that the beneficial effects of oxygen vacancies are conducive to the design of high-performance Li-rich cathodes for Li-ion batteries.

4. Experimental Section

Synthesis: $Li_5Mn_3O_8$ and $Li_5Mn_3O_{6.5}$ were synthesized using a mechanochemical method. Li_2O, Mn_3O_4, Mn_2O_3, and MnO_2 were used as precursors, and 5% excess Li_2O was used to compensate for possible loss of Li_2O during synthesis. Li_2O, Mn_2O_3, and MnO_2 at a molar ratio of 2.625:0.5:2 were used to prepare $Li_5Mn_3O_8$, and Li_2O and Mn_3O_4 at a molar ratio of 2.625:1 were used to prepare $Li_5Mn_3O_{6.5}$. The precursors were transferred into argon-filled stainless-steel jars (50 mL) and then planetary ball-milled for 40 h at 450 rpm using a Retsch PM 200. Five 10 mm-diameter and ten 5 mm-diameter stainless-steel balls were used as the grinding media. The same ball-mill procedure was used to synthesize $Li_5Mn_3O_6F$ and $Li_5Fe_3O_{6.5}$. Li_2O, LiF, and Mn_3O_4 at a molar ratio of 2.1:1:1 were used to prepare $Li_5Mn_3O_6F$, and Li_2O and Fe_3O_4 at a molar ratio of 2.625:1 were used to prepare $Li_5Fe_3O_{6.5}$.

Electrochemistry: The active material, carbon black (Timcal, SUPER C65), and polytetrafluoroethylene (PTFE; DuPont, Teflon 8A) were mixed at a weight ratio of 70:20:10 to prepare the cathode film. Specifically,

210 mg of the active material and 60 mg of carbon black were mixed and shaker-milled for 1 h in an argon atmosphere using a SPEX 800M mixer, and PTFE was then added to the mixture and manually mixed for 30 min. The three components were rolled into a thin film inside an argon-filled glove box. Coin cells were assembled using the cathode film, lithium metal foil, the electrolyte (1 M LiPF$_6$ in 1:1 volume ratio of ethylene carbonate [EC] and dimethyl carbonate [DMC] [BASF]), and separators (Whatman glass microfiber filter) in an argon-filled glove box. The loading density of active material was approximately 3 mg cm^{-2} for each cathode film. Galvanostatic cycling tests were performed at room temperature using an Arbin battery tester. Electrochemically delithiated/lithiated samples were prepared by charging/discharging the cells at a current density of 20 mA g^{-1}, and the charged/discharged cathode films were collected after washing with DMC in an argon-filled glove box.

Characterization: Synchrotron-based XRD was performed at beamline 11-ID-B at the Advanced Photon Source, Argonne National Laboratory. The beam was calibrated to a wavelength of 0.2113 Å. Lab XRD patterns were collected using a Bruker D8 ADVANCE diffractometer (Cu source) in the 2θ range of 10°–85°. Rietveld refinement was performed using the PANalytical X'pert HighScore Plus software. Thermogravimetric analysis (TGA) was conducted at a rate of 5 °C min^{-1} under an oxygen atmosphere using a TA instruments SDT Q600. SEM images were collected on a Zeiss Gemini Ultra-55 analytical field-emission scanning electron microscope with acceleration voltages of 5–10 kV.

Hard XAS: Mn K-edge XAS measurements were performed at 20-BM beamline at the Advanced Photon Source, Argonne National Laboratory. The measurements were collected in transmission mode using a Si (111) monochromator. Mn foil (6539 eV) was simultaneously measured with the experimental measurements to calibrate the energy of the individual data set. All the ex situ samples were sealed between polyimide tapes to avoid air exposure. The XAS spectra were calibrated and normalized using the Athena software package.[52,53] The background contribution was limited below $R_{bkg} = 1.0$ using the built-in AUTOBK algorithm. The normalized spectra were converted from energy to wave-vector k and then Fourier transformed from k-space to R-space to obtain the extended EXAFS spectra. Linear combination fits of the XANES spectra were performed using the Athena software package.

mRIXS: The O K-edge mRIXS data were collected at the iRIXS endstation at beamline 8.0.1 at the Advanced Light Source, Lawrence Berkeley National Laboratory. The samples were processed and mounted in an Ar glove box, then transferred to the experimental vacuum chamber using a sealed sample transfer kit to avoid any air exposure. Emission spectra were collected at every 0.2 eV excitation energy, with energy resolution of about 0.25 eV.

Computational Methods: DFT calculations were performed using the Vienna Ab initio Simulation Package (VASP)[54] using the projector-augmented wave method,[55] a plane-wave basis set with an energy cutoff equal to 520 eV, and a reciprocal space discretization of 25 K-points per Å. All the calculations were converged to 10^{-6} eV in total energy for electronic loops and 0.02 eV Å^{-1} in interatomic forces for ionic loops. We relied on the strongly constrained and appropriately normed (SCAN) meta-GGA exchange–correlation functional.[56] The SCAN functional is believed to better capture redox-related charge transfer, which would improve the accuracy of the energetics involving the introduction of anion vacancies.[57]

To compute the phase stability in the LMO-V system, a phase diagram of Li–Mn–O was constructed with all stable compositions predicted with prior GGA/GGA + U-DFT calculations from the Materials Project database.[58,59] We took the GGA/GGA + U predicted stable compounds as the inputs for SCAN-DFT calculations. These compounds were still the ground-state compounds in the SCAN-DFT phase diagram, with no missing stable compounds (Figure S8a, Supporting Information). This indicates the consistency of the stable entries in our phase diagram compared with prior calculations. All structure analysis and postprocessing were done using the pymatgen software package.[60]

To efficiently sample the thermodynamics of the Li_2O–Mn_3O_4 DRX compounds, a lattice cluster expansion was constructed. The cluster expansion technique is used to study the configurational thermodynamics

of materials in which sites can be occupied by multiple cations and has been applied to study the Li-vacancy configuration in layered materials[61] and the cation short-range order in DRX compounds.[45,46,62] In this Li_2O–Mn_3O_4 DRX system, the anion fcc lattice can be occupied by O^{2-} and vacancies, and the octahedral cation lattice can be occupied by Li and Mn. We fitted a cluster expansion model built from pair interactions up to 7.1 Å, triplet interactions up to 5.6 Å, and quadruplet interactions up to 4.2 Å based on a primitive cell of the rocksalt structure with $a = 3$ Å. The final effective cluster interactions (ECIs) were obtained using ℓ_1-norm regularized linear regression with the best regularization parameter selected to minimize the cross-validation (CV) score.[63,64] The root-mean-squared CV errors were converged to 5 meV atom^{-1}.

As the disordered rocksalt has large configurational degrees of freedom, we applied a canonical cluster expansion Monte Carlo (CEMC) simulation to sample the internal energy $E(T)$ and configurational entropy $S(T)$.[65] To identify the region at which the disordered phase of $Li_5Mn_3O_{6.5}$ is stable, the order–disorder transition temperature T_c was found from the maximum in the Monte Carlo heat capacity $C_v \propto \Delta E^2/T^2$. The result is denoted by the vertical red dashed line in Figure S8b, Supporting Information. A representative state of disordered $Li_5Mn_3O_{6.5}$ was selected at $T^* = T_c + 100$ (slightly above the critical point), and the free energy $F(T)$ of disordered $Li_5Mn_3O_{6.5}$ (LMO-V) was calculated as follows

$$F(T) = \begin{cases} E(T) - TS(T), & (T > T^*) \\ E(T^*) - TS(T^*), & (T < T^*) \end{cases} \tag{1}$$

The approximation for $T < T^*$ is necessary as Monte Carlo cannot track the free energy of the disordered state below its equilibrium ordering temperature. For this reason, the energy and entropy of the disordered state are fixed at the $T = T^*$ state (essentially assuming the configurational state does not vary) and the free energy becomes linear in temperature. The configurational entropy of $Li_5Mn_3O_{6.5}$ was integrated from infinite to finite temperature T by

$$S(T) = -k_B \left[\sum_{i=Li/Mn} c_i \ln c_i + \sum_{i=O/Vac} a_i \ln a_i \right] + \int_\infty^T \frac{C_v}{T} dT \tag{2}$$

where C_v is the heat capacity, k_B is the Boltzmann constant, and c_i/a_i is the concentration of cation/anion species in LMO-V, respectively.[65]

All Monte Carlo simulations on these cluster expansion Hamiltonians were performed in a canonical ensemble using Metropolis–Hastings sampling on a $8 \times 8 \times 6$ supercell (768 ions) of the primitive unit cell of the rocksalt structure. The canonical Monte Carlo was implemented by annealing from high $T = 10^5$ K to low $T = 50$ K. The internal energy $E(T)$ and fluctuation $\Delta E^2(T)$ was sampled from 1000 structures taken from the equilibrium ensemble at each temperature T. The configurational entropy was integrated from 10^5 K (for approximation of S_∞) to finite T using $S(T) = S_\infty + \int_\infty^T \frac{C_v}{T} dT$, where $S_\infty = -k_B \left[\sum_{i=Li/Mn} c_i \ln c_i + \sum_{i=O/Vac} a_i \ln a_i \right]$ is the ideal configurational entropy in the fully disordered limit.

Supporting Information

Supporting Information is available from the Wiley Online Library or from the author.

Acknowledgements

Conflict of Interest

The authors declare no conflict of interest.

Author Contributions

J.H. and G.C. planned the project. G.C. supervised all aspects of the research. J.H. synthesized, characterized, and electrochemically tested the proposed materials. P.Z. performed the theoretical calculations and analyzed the results. Y.H. collected and analyzed the RIXS data with W.Y. Y.T. performed the SEM characterization. Z.L. and M.B. helped with XAS data collection and analyses. The manuscript was written by J.H. and G.C. and was revised by the other co-authors. All the authors contributed to discussions.

Data Availability Statement

The data that support the findings of this study are available from the corresponding author upon reasonable request.

Keywords

[1] E. A. Olivetti, G. Ceder, G. G. Gaustad, X. Fu, *Joule* **2017**, *1*, 229.

[2] Z. Lu, D. D. MacNeil, J. R. Dahn, *Electrochem. Solid-State Lett.* **2001**, *4*, A191.

[3] J. Lee, A. Urban, X. Li, D. Su, G. Hautier, G. Ceder, *Science* **2014**, *343*, 519.

[4] J. Lee, D. A. Kitchaev, D.-H. Kwon, C.-W. Lee, J. K. Papp, Y.-S. Liu, Z. Lun, R. J. Clément, T. Shi, B. D. McCloskey, J. Guo, M. Balasubramanian, G. Ceder, *Nature* **2018**, *556*, 185.

[5] R. J. Clément, Z. Lun, G. Ceder, *Energy Environ. Sci.* **2020**, *13*, 345.

[6] A. Urban, J. Lee, G. Ceder, *Adv. Energy Mater.* **2014**, *4*, 1400478.

[7] N. Yabuuchi, M. Nakayama, M. Takeuchi, S. Komaba, Y. Hashimoto, T. Mukai, H. Shiiba, K. Sato, Y. Kobayashi, A. Nakao, M. Yonemura, K. Yamanaka, K. Mitsuhara, T. Ohta, *Nat. Commun.* **2016**, *7*, 13814.

[8] H. Ji, A. Urban, D. A. Kitchaev, D.-H. Kwon, N. Artrith, C. Ophus, W. Huang, Z. Cai, T. Shi, J. C. Kim, H. Kim, G. Ceder, *Nat. Commun.* **2019**, *10*, 592.

[9] J. Huang, P. Zhong, Y. Ha, D.-H. Kwon, M. J. Crafton, Y. Tian, M. Balasubramanian, B. D. McCloskey, W. Yang, G. Ceder, *Nat. Energy* **2021**, *6*, 706.

[10] A. R. Armstrong, M. Holzapfel, P. Novák, C. S. Johnson, S.-H. Kang, M. M. Thackeray, P. G. Bruce, *J. Am. Chem. Soc.* **2006**, *128*, 8694.

[11] S. Hy, H. Liu, M. Zhang, D. Qian, B.-J. Hwang, Y. S. Meng, *Energy Environ. Sci.* **2016**, *9*, 1931.

[12] E. Hu, X. Yu, R. Lin, X. Bi, J. Lu, S. Bak, K.-W. Nam, H. L. Xin, C. Jaye, D. A. Fischer, K. Amine, X.-Q. Yang, *Nat. Energy* **2018**, *3*, 690.

[13] R. A. House, J.-J. Marie, M. A. Pérez-Osorio, G. J. Rees, E. Boivin, P. G. Bruce, *Nat. Energy* **2021**, *6*, 781.

[14] J. Lee, J. K. Papp, R. J. Clément, S. Sallis, D.-H. Kwon, T. Shi, W. Yang, B. D. McCloskey, G. Ceder, *Nat. Commun.* **2017**, *8*, 981.

[15] D. Chen, W. H. Kan, G. Chen, *Adv. Energy Mater.* **2019**, *9*, 1901255.

[16] Z. Zhu, R. Gao, I. Waluyo, Y. Dong, A. Hunt, J. Lee, J. Li, *Adv. Energy Mater.* **2020**, *10*, 2001120.

[17] M. J. Crafton, Y. Yue, T.-Y. Huang, W. Tong, B. D. McCloskey, *Adv. Energy Mater.* **2020**, *10*, 2001500.

[18] Z. Lun, B. Ouyang, Z. Cai, R. J. Clément, D.-H. Kwon, J. Huang, J. K. Papp, M. Balasubramanian, Y. Tian, B. D. McCloskey, H. Ji, H. Kim, D. A. Kitchaev, G. Ceder, *Chem* **2020**, *6*, 153.

[19] Z. Zhuo, K. Dai, R. Qiao, R. Wang, J. Wu, Y. Liu, J. Peng, L. Chen, Y. Chuang, F. Pan, Z. Shen, G. Liu, H. Li, T. P. Devereaux, W. Yang, *Joule* **2021**, *5*, 975.

[20] J. Lee, D.-H. Seo, M. Balasubramanian, N. Twu, X. Li, G. Ceder, *Energy Environ. Sci.* **2015**, *8*, 3255.

[21] N. Yabuuchi, M. Takeuchi, M. Nakayama, H. Shiiba, M. Ogawa, K. Nakayama, T. Ohta, D. Endo, T. Ozaki, T. Inamasu, K. Sato, S. Komaba, *Proc. Natl. Acad. Sci* **2015**, *112*, 7650.

[22] N. Yabuuchi, M. Takeuchi, S. Komaba, S. Ichikawa, T. Ozaki, T. Inamasu, *Chem. Commun.* **2016**, *52*, 2051.

[23] M. Nakajima, N. Yabuuchi, *Chem. Mater.* **2017**, *29*, 6927.

[24] M. A. Cambaz, B. P. Vinayan, H. Euchner, S. A. Pervez, H. Geßwein, T. Braun, A. Gross, M. Fichtner, *ACS Appl. Mater. Interfaces* **2019**, *11*, 39848.

[25] R. Chen, S. Ren, M. Knapp, D. Wang, R. Witter, M. Fichtner, H. Hahn, *Adv. Energy Mater.* **2015**, *5*, 1401814.

[26] J. Ahn, D. Chen, G. Chen, *Adv. Energy Mater.* **2020**, *10*, 2001671.

[27] L. Li, Z. Lun, D. Chen, Y. Yue, W. Tong, G. Chen, G. Ceder, C. Wang, *Adv. Funct. Mater.* **2021**, *31*, 2101888.

[28] K. Zhou, S. Zheng, F. Ren, J. Wu, H. Liu, M. Luo, X. Liu, Y. Xiang, C. Zhang, W. Yang, L. He, Y. Yang, *Energy Storage Mater.* **2020**, *32*, 234.

[29] R. A. House, L. Jin, U. Maitra, K. Tsuruta, J. W. Somerville, D. P. Förstermann, F. Massel, L. Duda, M. R. Roberts, P. G. Bruce, *Energy Environ. Sci.* **2018**, *11*, 926.

[30] H. Hafiz, K. Suzuki, B. Barbiellini, N. Tsuji, N. Yabuuchi, K. Yamamoto, Y. Orikasa, Y. Uchimoto, Y. Sakurai, H. Sakurai, A. Bansil, V. Viswanathan, *Nature* **2021**, *594*, 213.

[31] D.-H. Seo, J. Lee, A. Urban, R. Malik, S. Kang, G. Ceder, *Nat. Chem.* **2016**, *8*, 692.

[32] P. M. Csernica, S. S. Kalirai, W. E. Gent, K. Lim, Y.-S. Yu, Y. Liu, S.-J. Ahn, E. Kaeli, X. Xu, K. H. Stone, A. F. Marshall, R. Sinclair, D. A. Shapiro, M. F. Toney, W. C. Chueh, *Nat. Energy* **2021**, *6*, 642.

[33] M. Freire, N. V. Kosova, C. Jordy, D. Chateigner, O. I. Lebedev, A. Maignan, V. Pralong, *Nat. Mater.* **2016**, *15*, 173.

[34] M. Freire, M. Diaz-Lopez, P. Bordet, C. V. Colin, O. I. Lebedev, N. V. Kosova, C. Jordy, D. Chateigner, A. L. Chuvilin, A. Maignan, V. Pralong, *J. Mater. Chem. A* **2018**, *6*, 5156.

[35] M. Diaz-Lopez, Y. Joly, M. Freire, C. Colin, O. Proux, V. Pralong, P. Bordet, *J. Phys. Chem. C* **2018**, *122*, 29586.

[36] A. Manceau, M. A. Marcus, S. Grangeon, *Am. Mineral.* **2012**, *97*, 816.

[37] S. Remsen, B. Dabrowski, *Chem. Mater.* **2011**, *23*, 3818.

[38] C. Abughayada, B. Dabrowski, M. Avdeev, S. Kolesnik, S. Remsen, O. Chmaissem, *J. Solid State Chem.* **2014**, *217*, 127.

[39] K. Luo, M. R. Roberts, R. Hao, N. Guerrini, D. M. Pickup, Y.-S. Liu, K. Edström, J. Guo, A. V. Chadwick, L. C. Duda, P. G. Bruce, *Nat. Chem.* **2016**, *8*, 684.

[40] J. Rana, J. K. Papp, Z. Lebens-Higgins, M. Zuba, L. A. Kaufman, A. Goel, R. Schmuch, M. Winter, M. S. Whittingham, W. Yang, B. D. McCloskey, L. F. J. Piper, *ACS Energy Lett.* **2020**, *5*, 634.

[41] W. Yang, T. P. Devereaux, *J. Power Sources* **2018**, *389*, 188.

[42] K. Dai, J. Wu, Z. Zhuo, Q. Li, S. Sallis, J. Mao, G. Ai, C. Sun, Z. Li, W. E. Gent, W. C. Chueh, Y. Chuang, R. Zeng, Z. Shen, F. Pan, S. Yan, L. F. J. Piper, Z. Hussain, G. Liu, W. Yang, *Joule* **2019**, *3*, 518.

[43] S. Kim, M. Aykol, V. I. Hegde, Z. Lu, S. Kirklin, J. R. Croy, M. M. Thackeray, C. Wolverton, *Energy Environ. Sci.* **2017**, *10*, 2201.

[44] P. K. Nayak, E. M. Erickson, F. Schipper, T. R. Penki, N. Munichandraiah, P. Adelhelm, H. Sclar, F. Amalraj, B. Markovsky, D. Aurbach, *Adv. Energy Mater.* **2018**, *8*, 1702397.

[45] R. J. Clément, D. Kitchaev, J. Lee, G. Ceder, *Chem. Mater.* **2018**, *30*, 6945.

[46] P. Zhong, Z. Cai, Y. Zhang, R. Giovine, B. Ouyang, G. Zeng, Y. Chen, R. Clément, Z. Lun, G. Ceder, *Chem. Mater.* **2020**, *32*, 10728.

[47] N. Tran, L. Croguennec, M. Ménétrier, F. Weill, P. Biensan, C. Jordy, C. Delmas, *Chem. Mater.* **2008**, *20*, 4815.

[48] B. Qiu, M. Zhang, L. Wu, J. Wang, Y. Xia, D. Qian, H. Liu, S. Hy, Y. Chen, K. An, Y. Zhu, Z. Liu, Y. S. Meng, *Nat. Commun.* **2016**, *7*, 12108.

[49] K. Kubota, T. Kaneko, M. Hirayama, M. Yonemura, Y. Imanari, K. Nakane, R. Kanno, *J. Power Sources* **2012**, *216*, 249.

[50] D. A. Kitchaev, Z. Lun, W. D. Richards, H. Ji, R. J. Clément, M. Balasubramanian, D.-H. Kwon, K. Dai, J. K. Papp, T. Lei, B. D. McCloskey, W. Yang, J. Lee, G. Ceder, *Energy Environ. Sci.* **2018**, *11*, 2159.

[51] D. Liu, C. Wang, Y. Yu, B.-H. Zhao, W. Wang, Y. Du, B. Zhang, *Chem* **2019**, *5*, 376.

[52] B. Ravel, M. Newville, *J. Synchrotron Radiat.* **2005**, *12*, 537.

[53] B. Ravel, M. Newville, *Phys. Scr.* **2005**, *T115*, 1007, https://doi.org/10.1238/Physica.Topical.115a01007.

[54] G. Kresse, D. Joubert, *Phys. Rev. B* **1999**, *59*, 1758.

[55] G. Kresse, J. Furthmüller, *Comput. Mater. Sci.* **1996**, *6*, 15.

[56] J. Sun, A. Ruzsinszky, J. P. Perdew, *Phys. Rev. Lett.* **2015**, *115*, 36402.

[57] D. A. Kitchaev, H. Peng, Y. Liu, J. Sun, J. P. Perdew, G. Ceder, *Phys. Rev. B* **2016**, *93*, 045132.

[58] A. Jain, S. P. Ong, G. Hautier, W. Chen, W. D. Richards, S. Dacek, S. Cholia, D. Gunter, D. Skinner, G. Ceder, K. A. Persson, *APL Mater.* **2013**, *1*, 011002.

[59] Z. Yao, S. Kim, J. He, V. I. Hegde, C. Wolverton, *Sci. Adv.* **2018**, *4*, eaao6754.

[60] S. P. Ong, W. D. Richards, A. Jain, G. Hautier, M. Kocher, S. Cholia, D. Gunter, V. L. Chevrier, K. A. Persson, G. Ceder, *Comput. Mater. Sci.* **2013**, *68*, 314.

[61] A. Van der Ven, M. Aydinol, G. Ceder, G. Kresse, J. Hafner, *Phys. Rev. B* **1998**, *58*, 2975.

[62] B. Ouyang, N. Artrith, Z. Lun, Z. Jadidi, D. A. Kitchaev, H. Ji, A. Urban, G. Ceder, *Adv. Energy Mater.* **2020**, *10*, 1903240.

[63] A. Walle, G. Ceder, *J. Phase Equilib.* **2002**, *23*, 348.

[64] L. J. Nelson, G. L. W. Hart, F. Zhou, V. Ozoliņš, *Phys. Rev. B* **2013**, *87*, 35125.

[65] W. D. Richards, S. T. Dacek, D. A. Kitchaev, G. Ceder, *Adv. Energy Mater.* **2018**, *8*, 1701533.